A dual-modality optical coherence tomography and fluorescence lifetime imaging microscopy system for simultaneous morphological and biochemical tissue characterization

Jesung Park, Javier A. Jo, Sebina Shrestha, Paritosh Pande, Qiujie Wan, and Brian E. Applegate*

Department of Biomedical Engineering, Texas A&M University, 337 Zachary Building, College Station, TX 77843, USA

*apple@tamu.edu

Abstract: Most pathological conditions elicit changes in the tissue optical response that may be interrogated by one or more optical imaging modalities. Any single modality typically only furnishes an incomplete picture of the tissue optical response, hence an approach that integrates complementary optical imaging modalities is needed for a more comprehensive non-destructive and minimally-invasive tissue characterization. We have developed a dual-modality system, incorporating optical coherence tomography (OCT) and fluorescence lifetime imaging microscopy (FLIM), that is capable of simultaneously characterizing the 3-D tissue morphology and its biochemical composition. The Fourier domain OCT subsystem, at an 830 nm center wavelength, provided high-resolution morphological volumetric tissue images with an axial and lateral resolution of 7.3 and 13.4 µm, respectively. The multispectral FLIM subsystem, based on a direct pulse-recording approach (upon 355 nm laser excitation), provided two-dimensional superficial maps of the tissue autofluorescence intensity and lifetime at three customizable emission bands with 100 µm lateral resolution. Both subsystems share the same excitation/illumination optical path and are simultaneously raster scanned on the sample to generate coregistered OCT volumes and FLIM images. The developed OCT/FLIM system was capable of a maximum A-line rate of 59 KHz for OCT and a pixel rate of up to 30 KHz for FLIM. The dual-modality system was validated with standard fluorophore solutions and subsequently applied to the characterization of two biological tissue types: postmortem human coronary atherosclerotic plaques, and *in vivo* normal and cancerous hamster cheek pouch epithelial tissue.

References and links

1. C. Balas, "Review of biomedical optical imaging-a powerful, non-invasive, non-ionizing technology for improving in vivo diagnosis," Meas. Sci. Technol. **20**(10), 104020 (2009).
2. C. Vinegoni, T. Ralston, W. Tan, W. Luo, D. L. Marks, and S. A. Boppart, "Integrated structural and functional optical imaging combining spectral-domain optical coherence and multiphoton microscopy," Appl. Phys. Lett. **88**(5), 053901 (2006).
3. J. K. Barton, F. Guzman, and A. Tumlinson, "Dual modality instrument for simultaneous optical coherence tomography imaging and fluorescence spectroscopy," J. Biomed. Opt. **9**(3), 618–623 (2004).
4. K. König, M. Speicher, R. Bückle, J. Reckfort, G. McKenzie, J. Welzel, M. J. Koehler, P. Elsner, and M. Kaatz, "Clinical optical coherence tomography combined with multiphoton tomography of patients with skin diseases," J Biophotonics **2**(6-7), 389–397 (2009).

5. C. A. Patil, N. Bosschaart, M. D. Keller, T. G. van Leeuwen, and A. Mahadevan-Jansen, "Combined Raman spectroscopy and optical coherence tomography device for tissue characterization," Opt. Lett. **33**(10), 1135–1137 (2008).
6. P. J. Caspers, G. W. Lucassen, and G. J. Puppels, "Combined in vivo confocal Raman spectroscopy and confocal microscopy of human skin," Biophys. J. **85**(1), 572–580 (2003).
7. A. R. Tumlinson, L. P. Hariri, U. Utzinger, and J. K. Barton, "Miniature endoscope for simultaneous optical coherence tomography and laser-induced fluorescence measurement," Appl. Opt. **43**(1), 113–121 (2004).
8. L. P. Hariri, A. R. Tumlinson, D. G. Besselsen, U. Utzinger, E. W. Gerner, and J. K. Barton, "Endoscopic optical coherence tomography and laser-induced fluorescence spectroscopy in a murine colon cancer model," Lasers Surg. Med. **38**(4), 305–313 (2006).
9. Z. G. Wang, D. B. Durand, M. Schoenberg, and Y. T. Pan, "Fluorescence guided optical coherence tomography for the diagnosis of early bladder cancer in a rat model," J. Urol. **174**(6), 2376–2381 (2005).
10. J. Fujimoto, and W. Drexler, *Introduction to Optical Coherence Tomography*, Optical Coherence Tomography: Technology and Applications (Springer, Berlin, Germany, 2008).
11. Y. Sun, R. Liu, D. S. Elson, C. W. Hollars, J. A. Jo, J. Park, Y. Sun, and L. Marcu, "Simultaneous time- and wavelength-resolved fluorescence spectroscopy for near real-time tissue diagnosis," Opt. Lett. **33**(6), 630–632 (2008).
12. S. Shrestha, B. E. Applegate, J. Park, X. Xiao, P. Pande, and J. A. Jo, "A Novel High-Speed Multispectral Fluorescence Lifetime Imaging Implementation for in vivo Applications," Opt. Lett. in press.
13. R. M. Clegg, *Fluorescence lifetime-resolved imaging*, FLIM microscopy in biology and medicine (CRC Press, Boca Raton, Fla., 2010).
14. D. N. Stephens, J. Park, Y. Sun, T. Papaioannou, and L. Marcu, "Intraluminal fluorescence spectroscopy catheter with ultrasound guidance," J. Biomed. Opt. **14**(3), 030505 (2009).
15. J. R. Lakowicz, H. Szmacinski, K. Nowaczyk, and M. L. Johnson, "Fluorescence lifetime imaging of free and protein-bound NADH," Proc. Natl. Acad. Sci. U.S.A. **89**(4), 1271–1275 (1992).
16. D. K. Bird, L. Yan, K. M. Vrotsos, K. W. Eliceiri, E. M. Vaughan, P. J. Keely, J. G. White, and N. Ramanujam, "Metabolic mapping of MCF10A human breast cells via multiphoton fluorescence lifetime imaging of the coenzyme NADH," Cancer Res. **65**(19), 8766–8773 (2005).
17. J. A. Jo, Q. Y. Fang, T. Papaioannou, and L. Marcu, "Fast model-free deconvolution of fluorescence decay for analysis of biological systems," J. Biomed. Opt. **9**(4), 743–752 (2004).
18. Q. Y. Fang, T. Papaioannou, J. A. Jo, R. Vaitha, K. Shastry, and L. Marcu, "Time-domain laser-induced fluorescence spectroscopy apparatus for clinical diagnostics," Rev. Sci. Instrum. **75**(1), 151–162 (2004).
19. S. T. Flock, S. L. Jacques, B. C. Wilson, W. M. Star, and M. J. C. van Gemert, "Optical properties of Intralipid: a phantom medium for light propagation studies," Lasers Surg. Med. **12**(5), 510–519 (1992).
20. J. L. Brandon, C. J. Conti, L. S. Goldstein, J. DiGiovanni, and I. B. Gimenez-Conti, "Carcinogenic effects of MGP-7 and B[a]P on the hamster cheek pouch," Toxicol. Pathol. **37**(6), 733–740 (2009).
21. P. Thomas, P. Pande, F. Clubb, J. Adame, and J. A. Jo, "Biochemical imaging of human atherosclerotic plaques with fluorescence lifetime angioscopy," Photochem. Photobiol. **86**(3), 727–731 (2010).
22. K. Arakawa, K. Isoda, T. Ito, K. Nakajima, T. Shibuya, and F. Ohsuzu, "Fluorescence analysis of biochemical constituents identifies atherosclerotic plaque with a thin fibrous cap," Arterioscler. Thromb. Vasc. Biol. **22**(6), 1002–1007 (2002).
23. L. Marcu, J. A. Jo, Q. Fang, T. Papaioannou, T. Reil, J. H. Qiao, J. D. Baker, J. A. Freischlag, and M. C. Fishbein, "Detection of rupture-prone atherosclerotic plaques by time-resolved laser-induced fluorescence spectroscopy," Atherosclerosis **204**(1), 156–164 (2009).
24. N. G. Ghoshal, and H. S. Bal, "Histomorphology of the hamster cheek pouch," Lab. Anim. **24**(3), 228–233 (1990).
25. D. G. Farwell, J. D. Meier, J. Park, Y. Sun, H. Coffman, B. Poirier, J. Phipps, S. Tinling, D. J. Enepekides, and L. Marcu, "Time-resolved fluorescence spectroscopy as a diagnostic technique of oral carcinoma: Validation in the hamster buccal pouch model," Arch. Otolaryngol. Head Neck Surg. **136**(2), 126–133 (2010).

1. Introduction

Early detection of pathological changes in biological tissues is key to early clinical diagnosis and subsequent reduction in the morbidity and mortality of numerous diseases. For many diseases the current standard of care for early detection is inadequate. For instance, invasive biopsy and histopathological analysis is the current gold standard for the early detection of pathological changes in cancer. Patient discomfort and tissue destruction hinders the biopsying of large areas of tissue, thus lowering the overall sensitivity of the technique. In addition, the labor intensive and time consuming preparation and analysis of the tissue precludes real time feedback to the clinician.

Optical imaging is a promising technique for the early detection of pathological changes since real-time and high fidelity optical images can be minimally or non-invasively acquired quickly over relatively large areas. Moreover, since the tissue can be interrogated *in vivo*, optical imaging has access to information that cannot be garnered from the histopathological analysis of dead tissue. Changes in elastic/inelastic scattering, absorption and emission can be

measured optically and used to infer pathological changes in the tissue morphology, biochemistry, and biomechanics. Unfortunately no one optical imaging modality is capable of measuring all of the changes in the optical response of pathological tissue.

Individual optical imaging modalities are typically only sensitive to a small part of the change in optical response. For instance, optical coherence tomography and microscopy measure the backward scattered light from tissue, and generate a morphological structural image. Fluorescence imaging acquires fluorescence emission from the different biochemical constituents of tissue to generate maps of the tissue biochemistry. White light polarimetry measures the polarization of scattered light to infer bio-mechanical tissue structure [1]. All three illustrative techniques glean valuable information from the interaction of light with tissue, yet they are not capable of a comprehensive measurement of the optical response.

A great deal of research effort has been applied to utilizing the individual optical imaging modalities to differentiate between healthy and diseased tissues. While the results have been promising in many cases, the complexity of pathological variation limits accurate early diagnosis by a single modality. Combination of two or more optical imaging modalities is necessitated to interrogate a larger segment of the optical response and increase sensitivity and specificity for early diagnosis. This strategy has recently been adopted by a number of researchers who have developed multi-modal systems combining optical coherence and multiphoton microscopy [2], optical coherence tomography (OCT) and fluorescence spectroscopy [3], OCT and multiphoton tomography [4], OCT and Raman spectroscopy [5], confocal Raman spectroscopy and confocal microscopy [6]. A major obstacle to combining many optical imaging modalities is the disparate optical requirements, including vastly different optical wavelengths.

The combination of OCT and fluorescence imaging is particularly compelling because they provide complementary information, tissue morphology and biochemistry. Several groups have investigated the combination of OCT with fluorescence imaging. Barton et al. [3] showed the diagnostic capacity of OCT and laser induced fluorescence spectroscopy for atherosclerotic plaques. Barton and associates [7,8] also developed a dual-modality miniature endoscope and imaged the gastrointestinal tract in a murine model of colon cancer. Wang et al. [9] combined OCT and fluorescence imaging for early bladder cancer diagnosis using a rat model. They obtained 79% sensitivity and 53% specificity when only the fluorescence image was analyzed, however when the analysis incorporated information gleaned from both OCT and fluorescence imaging the sensitivity and specificity were improved to 100% and 81%, respectively.

Here we report the development of a dual-modality OCT and Fluorescence Lifetime Imaging Microscopy (FLIM) system. Fourier domain OCT exploits low coherence spectral interferometry to generate a line image from each acquired spectrum that depicts the depth resolved tissue reflectivity (scattering) with micron scale resolution. High-speed spectrometers enable raster scanned volumetric images to be generated in a seconds or less. OCT has already been deployed in the clinic as a diagnostic tool in ophthalmology (retinal and anterior segment imaging) and more recently in cardiology (intravascular artery imaging) [10].

Multispectral FLIM, as implemented here, directly measures the fluorescence temporal decay at multiple wavelengths by exciting with a high repetition rate pulsed UV laser and recording the emission on a high-speed microchannel plate photomultiplier tube (MCP-PMT) and high speed digitizer. As we have shown previously [11,12], this approach can achieve high pixel rates only limited by the laser repetition rate, hence a raster scanned 2-D FLIM data set may be acquired in approximately the same time as required for an OCT volume. Moreover, we have chosen FLIM over simple fluorescence imaging because the fluorescence lifetime measurement is less sensitive to intensity artifacts, photo-bleaching, light scattering and excitation intensity, which makes it more robust for clinical applications [13].

For instance a significant intensity artifact arises from blood attenuation. Blood (oxyhemoglobin) has strong absorption bands at ~400 nm, ~540 nm, and ~570 nm, hence it diminishes the fluorescence intensities of endogenous fluorophores (e.g. collagen and elastin)

over those bands. In contrast, the fluorescence lifetime measurement is independent of relative intensity among spectral bands and is therefore not affected by the presence of blood [14].

The fluorescence lifetime is also more sensitive than fluorescence intensity to the local micro-environment. For instance, it has been shown that NADH and FAD in their free and protein-bound conditions present distinct lifetimes [15]. The free and bound NADH molecules have fluorescence lifetimes of ~0.5 ns and ~2-3 ns, while their emission spectra are very similar both with maximum excitation/emission at ~340/450 nm. The free and bound FAD molecules have the fluorescence lifetimes of ~1 ns and ~3-4 ns, with maximum excitation/emission of ~450/525 nm. The concentration ratio of free and bound NADH estimated using fluorescence lifetimes has been suggested as a nondestructive optical indicator for dysplastic metabolic changes [16].

The system performance was validated by acquiring and analyzing OCT/FLIM images of capillary tubes filled with fluorophore solutions and submersed in a scattering medium. Following validation we commenced the investigation of OCT/FLIM as an avenue to noninvasive early diagnosis of oral cancer and minimally invasive characterization of atherosclerotic plaques. We present early findings from both on-going studies.

2. Materials and methods

2.1 OCT/FLIM dual-modality imaging system

A schematic diagram of the dual-modality imaging system is shown in Fig. 1. The diagram can be divided into three sub-diagrams: OCT subsystem, FLIM subsystem, and Common Path. The solid black arrows indicate the optical path of the reference and sample arms of the
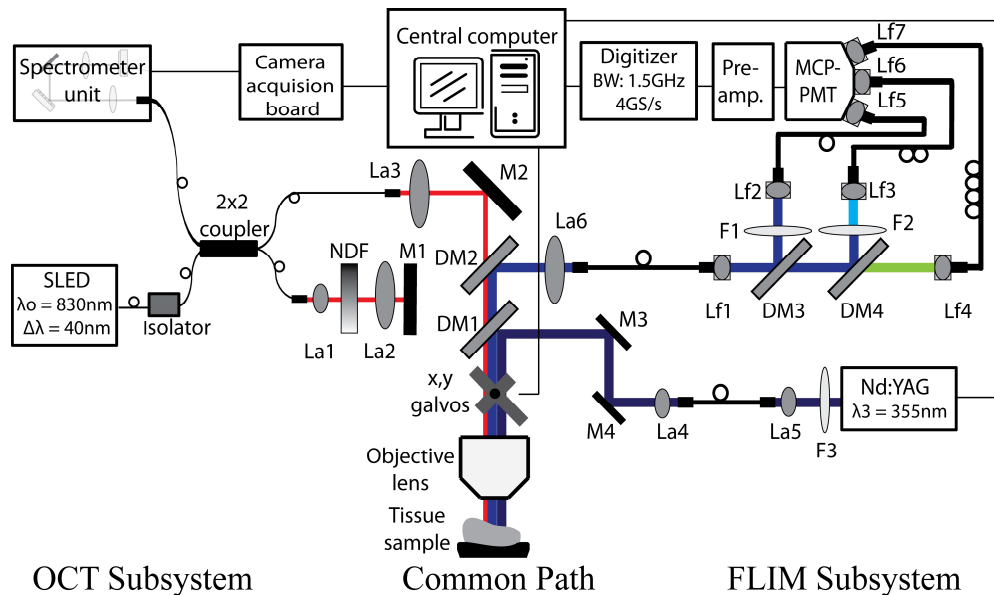

Fig. 1. Schematic diagram of the dual-modality imaging system. La1-La5: free-space collimation and coupling lenses, Lf1-Lf7: fiber-connected collimation and coupling lenses, NDF: neutral density filter, M1-M4: mirrors, DM1-DM4: dichroic mirrors, and F1-F3: filters

OCT module. The dashed gray arrows show the FLIM excitation light path, and the solid gray arrows show the FLIM fluorescence emission optical path. The connection between a central computer and all electronics and interfaces is symbolized by a thin solid black line.

2.2 OCT subsystem

A fiber-based Fourier domain OCT system was implemented as the OCT module. The light source was a superluminescent light emitting diode (SLED) (EXS8410-2413, Exalos,

Langhome, PA) with a center wavelength of 830 nm and spectral bandwidth of 40 nm, providing a coherence length (or axial resolution) of 7.3 µm in air. The SLED light propagated into an isolator (AC Photonics, Santa Clara, CA) designed to protect the light source from unwanted back reflections. Light exciting the isolator through single-mode optical fiber (AC Photonics, Santa Clara, CA) was divided by a 2x2 (50/50) single-mode coupler (AC Photonics, Santa Clara, CA) and directed to the reference and sample arms. The reflected beam from a reference mirror in the reference arm and the backscattered light from the sample were recombined at the coupler and generated a spectral interferogram on a custom designed high-speed spectrometer. The spectrometer was based around a transmissive grating (1200 L/mm, Wasatch Photonics, Logan, UT) and a CCD linescan camera (Aviiva, SM2CL1014, EV2 Technologies, Essex, England) capable of lines rates of up to 59 KHz with a minimum integration time of 5 µs. The detected signal was digitally converted and acquired by a high speed imaging acquisition board (PCIe-1427, National Instruments, Austin, TX). The OCT subsystem had a signal-to-noise ratio (SNR) of 98 dB and a 3 dB single sided fall-off of 900 µm.

The sample arm of the interferometer is encompassed in the Common Path in the OCT/FLIM System will be described in detail below.

2.3 FLIM subsystem

A scanning direct pulse-recording FLIM implementation was adopted for the FLIM module. A frequency tripled (355 nm) Q-switched Nd:YAG laser (SPOT-10-50-355, Elforlight Ltd., England) with a pulse width of 1 ns, maximum pulse energy of 5µJ and maximum repetition rate of 50 KHz was used as an excitation light source. A 50 µm multi-mode fiber delivered the excitation light to the OCT-FLIM Common Path.

The emission light exiting the OCT-FLIM Common Path was directed through a 200 µm multi-mode fiber into a multi-spectral detection module. The multi-spectral detection module was introduced for real-time time-resolved fluorescence spectroscopy [11]. We have recently adapted this multispectral detection module design for *in vivo* FLIM imaging [12]. We have taken the same approach for the FLIM module of the dual-modality imaging system. Three fluorescence decays at three different emission bands (390 +/− 20, 452 +/− 22.5 and 600 +/−125 nm) in the multispectral detection module was produced by using a set of dichroic mirrors and filters (Chroma Technology, Bellows Falls, VT). These bands were temporally separated by propagating each band through a different length (1, 10, or 19 m) of multimode fiber which imparted a 45 ns time delay between each band. The emission bands and fiber lengths were selected to detect tissue endogenous fluorophores, such as flavin adenine dinucleotide (FAD), nicotinamide adenine dinucleotide (NADH), collagen, elastin and lipids. Upon a single pulse excitation, the three fluorescence decays were simultaneously detected by a MCP-PMT with 150 ps rise time (R3809U-50, Hamamatsu, Japan) and amplified using a high-bandwidth pre-amplifier (1.5 GHz bandwidth, C5594, Hamamatsu, Japan). Finally, the sequence composed of the three consecutive decays was digitized at 4 GS/s using a PCI-ADC card (1.5 GHz analog bandwidth, CS14G8 CobraMax, GaGe, Lockport, IL).

A spectral intensity calibration was performed on the three spectral bands in order to compensate for wavelength dependent losses in the detection system and the PMT sensitivity. Images of capillary tubes containing POPOP and NADH were recorded. Both have appreciable intensity in the three bands. The spectra of POPOP and NADH were also recorded with a spectrometer recently calibrated with a NIST traceable quartz-tungsten-halogen calibration lamp. The average intensity over the bands noted above was calculated from the high resolution spectra. A normalized calibration coefficient (0.795@390 nm, 1@452 nm, 0.779@600 nm) was then determined for each band which brought the intensities measured with the FLIM subsystem into agreement with the average intensities from the spectrometer. For a more detailed description and discussion of the FLIM subsystem see [11,12].

2.4 Common path in OCT/FLIM system

The true integration of the OCT and FLIM subsystems takes place in the common optical path that is used to illuminate and scan the sample. The OCT sample beam and FLIM excitation were combined via a dichroic mirror (DM1) which was highly reflective in the UV and passed vis-nearIR light. The copropogating beams passed through a set of galvo mirrors (6230H, Cambridge Technology, Lexington, MA) used to raster scan the sample. A broadly achromatic (UV-nearIR) objective lens (5X/0.16 NA, EC plan-Neufluar, Zeiss, Germany) was used to simultaneously focus the OCT sample beam and FLIM excitation resulting in lateral resolutions of 13.4 µm for OCT and 100 µm for FLIM. The powers of the OCT beam and FLIM excitation light on the sample were 0.6 and 3.3 mW, respectively. The fluorescence emission was directed into the detection module by a second dichroic mirror (DM2) placed between the fiber collimating optics of the OCT sample beam and DM1. The mirror was highly reflective in the UV-vis range and passed nearIR.

2.5 System control and data processing

An OCT/FLIM data acquisition program written in Labview (Labview8.6, National Instruments, Austin, TX) was developed to control the electronics, data acquisition boards and imaging parameters. The program sent synchronized trigger signals to both the FLIM laser and the OCT camera, so that a pixel fluorescence decay acquisition coincides with the corresponding OCT A-line collection. 2-D FLIM decay data and co-registered 3-D OCT volume data were acquired after a controlled raster scan with two galvanometers, and saved into the central main computer.

Due to the low pulse energy of the current FLIM laser (maximum of 240 nJ at 10 KHz), tissue autofluorescence decays resulting from a single laser pulse excitation had an inadequate signal-to-noise-ratio (SNR). To improve the SNR of the FLIM signal, multiple fluorescence decays at a given pixel were acquired with multiple excitation laser pulses, and the decays were averaged. The FLIM maps of the *ex vivo* artery and *in vivo* hamster pouch used 20 fluorescence decays to represent one pixel.

Each Fourier domain OCT A-line was processed in the standard way using Matlab (Matlab R2007a, The Mathworks, Inc., Natick, MA); convert from λ to k-space, resample, and fast Fourier transform to get the depth resolved tissue reflectivity. In the context of time-domain FLIM data analysis, the measured fluorescence decay at each pixel of the image corresponds to the time convolution of the instrument response with the intrinsic fluorescence decay at that pixel. Therefore, to estimate the intrinsic fluorescence decay at each pixel of the image, the instrument response needs to be deconvolved from the measured pixel fluorescence decay. A recently proposed and validated deconvolution method based on the orthogonal expansion of the intrinsic fluorescence decays on a set of Laguerre functions was applied [17]. The Laguerre deconvolution method allowed for almost real-time estimation of the intrinsic fluorescence decays at each pixel of the FLIM images. After deconvolution, intensity maps for each band were computed by integrating over time the intrinsic fluorescence decay at each pixel. Then, the normalized fluorescence intensity maps were calculated by dividing (pixel-by-pixel) the intensity of each emission band by the sum of the intensity of all three bands. Thus, the 2-D normalized fluorescence intensity maps indicate the relative fluorescence intensity emitted at each band. To estimate the 2-D lifetime maps, the average lifetime was computed from the estimated pixel intrinsic fluorescence decay. The OCT volume and FLIM maps were fused by overlaying the 3-D OCT volume with 2-D FLIM maps. The fused OCT/FLIM data were rendered using ImageJ (1.42q, NIH, Bethesda, MA).

2.6 Sample preparation and imaging

2.6.1 Capillary tubes filled with fluorophores in Intralipid

Three standard fluorophores with known emission spectra and lifetimes were selected to evaluate the OCT/FLIM dual-modality system: POPOP in ethanol (Emission peak = 390 nm, lifetime = 1.2 - 1.5 ns), NADH in PBS (Emission peak = 450 nm, lifetime = 0.3 - 0.4 ns), and

FAD in PBS (Emission peak = 540 nm, lifetime = 2.3 - 2.85 ns) [18]. The fluorophore concentrations (0.015 mM in POPOP, 0.5 mM in NADH, and 1 mM in FAD) were chosen such that the peak emission intensity from each fluorophore was comparable. The dye samples were loaded into three quartz capillary tubes (ID = 300 µm, OD = 400 µm, and Length = 2500 µm). The capillary tubes were sealed to prevent leakage of dyes and were collaterally placed in 2% intralipid which is commonly used to mimic tissue light scattering [19]. The capillary tubes were placed ~100 µm below the surface of the intralipid and imaged. No averaging was performed, since the fluorescence efficiencies of the dyes were high enough even with a single excitation laser pulse at a pulse repetition rate of 30 kHz.

2.6.2 *Ex vivo* human coronary artery

Postmortem human coronary artery specimens were obtained within 40 hours from the time of the autopsy, according to a protocol approved by the Texas A&M University Institutional Review Board. The artery specimens were longitudinally opened to acquire OCT/FLIM images from the internal lumen side. For imaging, the specimens were placed on a quartz slide to minimize background fluorescence signal, and moistened to prevent it from drying during the experiment. The imaged artery samples were processed following standard procedures for histopathology analysis.

2.6.3 *In vivo* hamster cheek pouch

The OCT/FLIM dual-modality system was also being evaluated for the early detection of oral cancer lesions using a Syrian (Golden) hamster cheek pouch model of epithelial cancer. Following a previously reported protocol [20], epithelial cancer was induced by treating one cheek pouch of each hamster with a suspension of 2.0% Benzo[a]pyrene (Sigma Aldrich Corporation, St. Louis MO) in mineral oil three times per week for up to 32 weeks. Control hamsters were similarly treated with mineral oil only. The treatment and imaging protocol was approved by the Institutional Animal Care and Use Committee at Texas A&M University.

For imaging, the hamster was anesthetized with a cocktail of ketamine (Bioniche pharma USA, Lake Forest, IL) and xylazine (Akorn. Inc., Decatur, IL). After placing the hamster on a small lab jack-typed table, the cheek pouch was exposed to the air and positioned under the objective lens of the OCT/FLIM system. Co-registered OCT images and FLIM maps of 2x2 mm^2 tissue sections were simultaneously acquired at cancer-suspicious locations, which were thereafter marked with ink for identification with the tissue histopathology. The heart rate and oxygen saturation of the hamster were continuously monitored during the imaging procedure using a compact veterinary monitor (PC-VetGrad[+TM], Vmed Technology, Mill Creek, WA). After imaging, the hamster was euthanized using nembutal (Hospira, Inc., Lake Forest, IL), and biopsy samples from the imaged locations were taken for H&E histopathology analysis.

3. Results

3.1 Capillary tubes filled with fluorophores in Intralipid

The OCT/FLIM dual-modality system was first validated by imaging three capillary tubes loaded with POPOP, NADH and FAD placed within 2% intralipid (Fig. 2). The OCT/FLIM images were acquired with a pixel rate of 30 KHz. Figure 2(a-b) shows a 3-D OCT volume and a 2-D OCT B-scan image of the capillary tubes (2500 (x) x 2500 (y) x 600 (z) µm). The relative scale on the x, y and z axes in Fig. 2 was chosen to improve the visualization of the OCT/FLIM image. The circular structure in Fig. 2 represents the ends of the capillary tubes, which essentially show up as a void in the typical speckle pattern produced by the intralipid. Moreover, the inner diameter (305 µm), outer diameter (400 µm), the depth position (~100 µm) from the surface and separation distance between tubes (~750 µm) may be gleaned from the structural OCT image.

Normalized fluorescence intensity and lifetime maps are displayed in Fig. 2(c-d). The intensity and the lifetime values were calculated within the capillary tubes only, and the

averaged lifetime values were calculated only when the normalized fluorescence intensities in each band were greater than 0.1. The capillary tubes containing POPOP, NADH, and FAD could be identified based on their emission strength and lifetime in each band. POPOP in the leftmost tube showed peak emission intensity at 390 nm, and had a lifetime of 1.42 ± 0.01 ns. Likewise, the maximum emission of NADH in the middle tube was observed at 450 nm, and the lifetime was 0.36 ± 0.01 ns. FAD within the rightmost tube had the maximum emission at 550 nm with a lifetime of 2.47 ± 0.02 ns. The peak emission and lifetimes determined for each fluorophore was in good agreement with the literature [18].
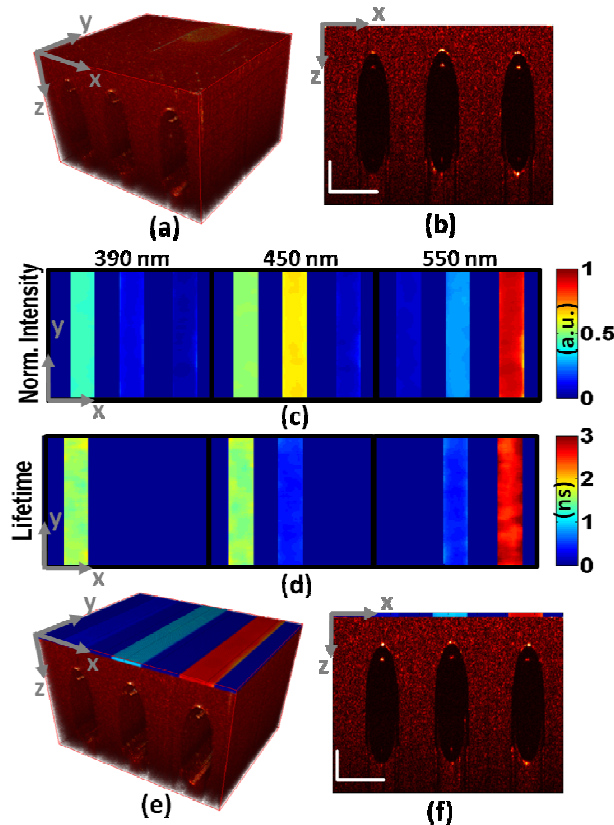
Fig. 2. Dual-modal OCT and FLIM images of three capillary tubes loaded with POPOP (left tube), NADH (center tube) and FAD (right tube) within the 2% intralipid (2500 (x) x 2500 (y) x 600 (z) µm). (a) 3-D OCT volume, (b) 2-D OCT B-scan, (c) Normalized fluorescence intensity maps, (d) Fluorescence lifetime maps, (e) 3-D OCT/FLIM volume with fluorescence intensity at the 550 nm band and (f) 2-D OCT/FLIM B-scan image with fluorescence intensity at the 550 nm band. Horizontal scale bar = 500 µm and vertical scale bar = 100 µm. A movie showing 3D nature of OCT/FLIM volume: (Media 1).

We have also started to investigate different strategies for displaying the dual-modal data sets. Figure 2(e-f) is one such strategy where the fluorescence intensity map (from the 550 nm band) has been projected onto the surface of the corresponding OCT volume or cross-section. Similarly, lifetime images could also be superimposed onto the OCT image to provide structural context to the biochemical information.

3.2 Ex vivo human coronary artery

Two examples of multimodal imaging of human coronary atherosclerotic plaques are presented here. The first example corresponds to a thin fibrotic plaque, and it is shown in Fig.

3. The OCT volume with a size of 2000 (x) x 2000 (y) x 350 (z) µm showed a fairly flat surface and three discernible layers (Fibrotic plaque in Intima (FP), Media (M) and Adventitia
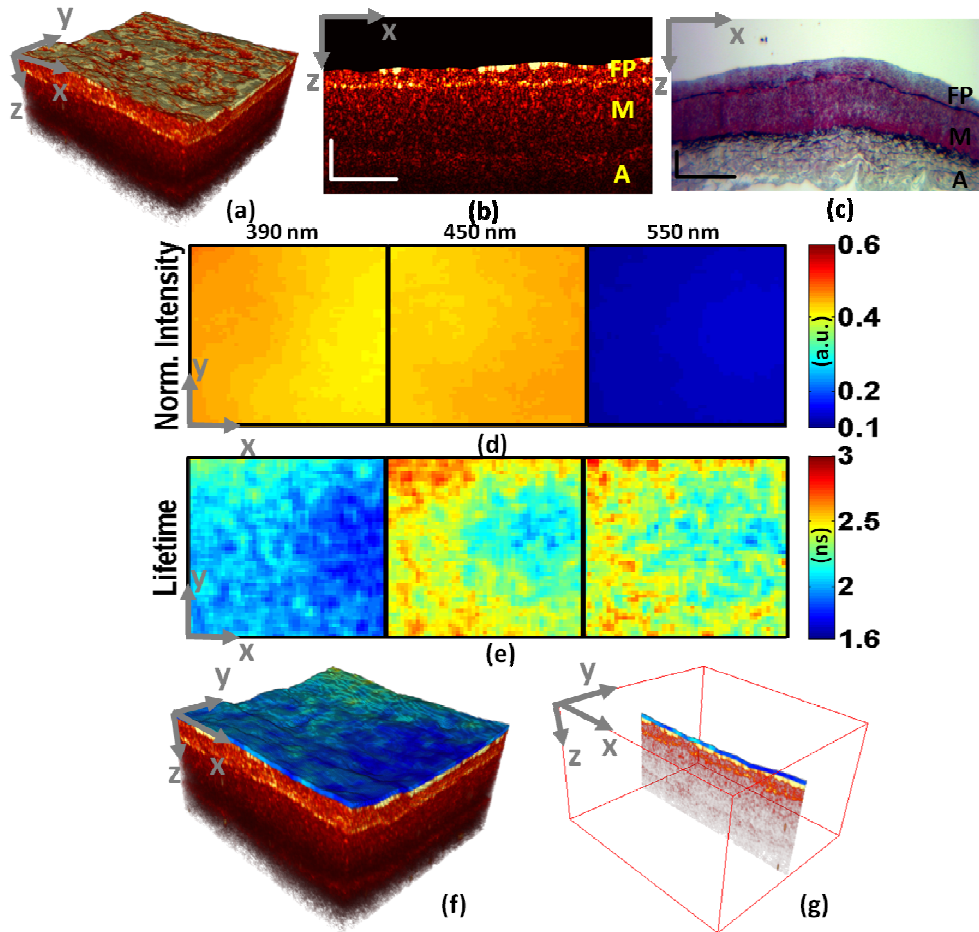

Fig. 3. Dual-modal OCT and FLIM images of an *ex vivo* human atherosclerotic artery tissue with thin fibrotic plaque (2000 (x) x 2000 (y) x 350 (z) µm). (a) 3-D OCT volume, (b) 2-D OCT B-scan (FB: Fibrotic plaque in Intima, M: Media and A: Adventitia), (c) H&E histology corresponding to (b), (d) Normalized fluorescence intensity maps, (e) Fluorescence lifetime maps, (f) 3-D OCT/FLIM volume with fluorescence lifetime in 390 nm band, and (g) Ortho-sliced image from (f). Horizontal scale bar = 400 µm and vertical scale bar = 100 µm. Movies showing 3D nature of OCT/FLIM volume: Media 2 and Media 3.

(A)) (Fig. 3(a)). The thicknesses of the layers (FP = ~50 µm and M = ~165 µm) could also be quantified in the cross-sectional OCT B-scan (Fig. 3(b)), assuming an average refractive index of 1.4. These morphological features were in agreement with the corresponding plaque histology (Fig. 3(c)).

Normalized fluorescence intensity and lifetime maps are displayed in Fig. 3(d-e). The normalized intensity maps reflected a broad emission spectrum covering the 390 nm and 450 nm emission bands, while the fluorescence lifetime maps showed short lifetimes (~2.00 ns) at the 390 nm band and longer lifetimes (~2.37 ns) at the longer emission bands. These features of the autofluorescence emission of the thin fibrotic plaque resemble the fluorescence of elastin found in the media layer. Since the amount of collagen in the thin plaque is relatively lower than that of elastin in the media, tissue autofluorescence is expected to be dominated by the elastin emission as observed.

The FLIM superficial maps can be superimposed over the OCT volumes to provide a comprehensive characterization of the atherosclerotic plaque. For instance, in Fig. 3(f-g) we show the fluorescence lifetime map from the 390 nm band overlaid over the corresponding OCT volume and an ortho-sliced image. These multimodal images provide an integrated representation of the underlying morphology and biochemical composition of a thin fibrotic atherosclerotic plaque.

The second example corresponds to a thick fibroatheroma presenting a thick fibrotic cap (TFC) overlaying a large calcified necrotic core (CNC), shown in Fig. 4. The OCT volume (2000 (x) x 2000 (y) x 650 (z) µm) in Fig. 4(a) showed a fairly uniform surface, a large core at the middle of the imaged section, and a thick section towards the right side of the volume. Structural evaluation of the artery tissue was performed on the cross-sectional OCT B-scan image (Fig. 4(b)). Averaged thickness of fibrotic cap (~125 µm) and spatial location and extension of the necrotic-core under the cap were clearly assessed based on the backscattering contrast between the cap and the necrotic-core, assuming the average tissue refractive index of 1.4. The corresponding plaque histology (Fig. 4(c)) confirmed the morphology of this lesion assessed by OCT (Fig. 4(b)).

The multispectral FLIM maps of the normalized fluorescence intensity and the lifetime of the thick cap fibroatheroma are shown in Fig. 4(d-e). Two different areas were observed in all FLIM maps that could be correlated to the fibroatheroma region (left) and to a mostly fibrotic region (right). The fibrotic region (right) showed stronger normalized fluorescence emission at the 390 nm band (~55%), followed by the 450 nm (~35%) and the 550 nm (~10%) bands; the fluorescence lifetime was longer (~2.6 ns) at the 390 nm band than at the 450 nm (~2.4 ns) and 550 nm (~2.0 ns) bands. These fluorescence characteristics resemble the emission of collagen, which is the dominant fluorophore in fibrotic plaques [21]. The fibroatheroma region (left) showed similar normalized fluorescence intensities at the 390 nm (~40%) and 450 nm (~45%) bands, and lower intensity at the 550 nm band (~15%); the fluorescence lifetime at all bands were bellow 1.8 ns. These fluorescence characteristic resemble the emission of lipids, which is abundant inside the necrotic core [22,23].

In Fig. 4(f-g) we also show the fluorescence lifetime map from the 390 nm band overlaid over the corresponding OCT volume of the thick cap fibroatheroma, and an ortho-sliced image. In these multimodal images we can clearly see two distinct regions of the plaque showing distinct morphology and biochemical composition, which are in agreement with the histopathological characteristics of a fibroatheroma and a fibrotic lesion.
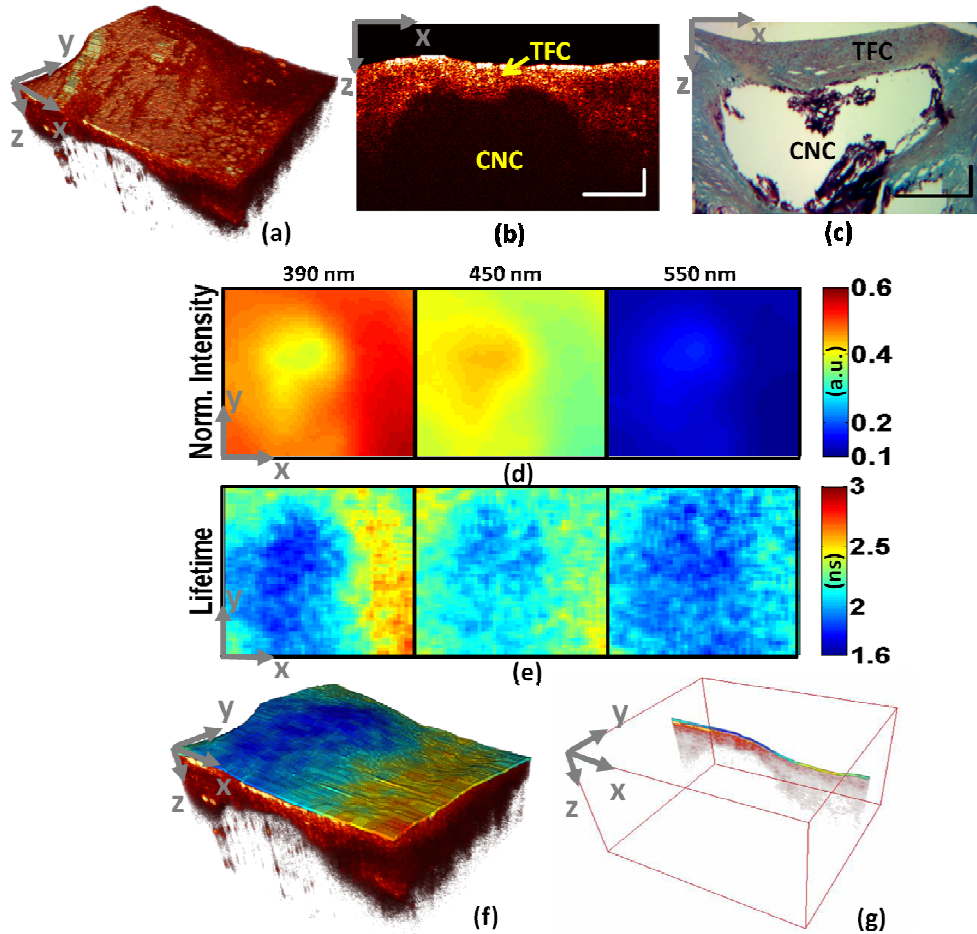
Fig. 4. Dual-modal OCT and FLIM maps of an *ex vivo* calcified human atherosclerotic artery tissue (2000 (x) x 2000 (y) x 650 (z) µm). (a) 3-D OCT volume, (b) 2-D OCT B-scan (TFC: thick fibrotic cap, CNC: calcified necrotic core), (c) H&E histology corresponding to (b), (d) Normalized fluorescence intensity maps, (e) Fluorescence lifetime maps, (f) 3-D OCT/FLIM volume with fluorescence lifetime in 390 nm band, and (g) Ortho-sliced image from (f). Horizontal scale bar = 400 µm and vertical scale bar = 100 µm. Movies showing 3D nature of OCT/FLIM volumes: Media 4 and Media 5.

3.3 In vivo hamster cheek pouch

Two examples of *in vivo* multimodal imaging of the hamster cheek pouch epithelial tissue are presented here. The first example corresponds to a normal oral mucosa, shown in Fig. 5. The OCT volume (Fig. 5(a)) with a size of 2000 (x) x 2000 (y) x 350 (z) µm showed a fairly smooth surface, a blood vessel running at the bottom of the tissue segment, and four discernible layers (Keratinized stratified squamous epithelium (KE), subepithelial connective tissue (lamina propria) (SC), skeletal muscle layer (tunica muscularis) (SM) and adventitial connective tissue (AC) [24]). The position and size of the blood vessel (BV) and the thicknesses of the layers (KE = ~20 µm, SC = ~80 µm and SM = ~140 µm) could also be quantified in the cross-sectional OCT B-scan (Fig. 5(b)), assuming an average refractive index of 1.4. These morphological features were in agreement with the corresponding normal oral mucosa histology (Fig. 5(c)).

Normalized fluorescence intensity and lifetime maps are displayed in Fig. 5(d-e). The normalized fluorescence intensity maps were quite homogeneous, with the 390 nm band

showing the stronger emission (~55%), followed by the 450 nm (~35%) and the 550 nm (~10%) bands; the fluorescence lifetime was longer (~3.5 ns) at the 390 nm band than at the 450 nm (~1.5 ns) and 550 nm (~1.5 ns) bands. These fluorescence characteristics resemble the emission of collagen, which is the dominant fluorophore in the normal oral mucosa [25].

In Fig. 5(f-g) we show the fluorescence lifetime map from the 390 nm band overlaid over the corresponding OCT volume, and an ortho-sliced image of the thin oral mucosa. In these multimodal images we can clearly see that both the tissue morphology and biochemical composition is fairly uniform within the imaged segment of normal oral mucosa.
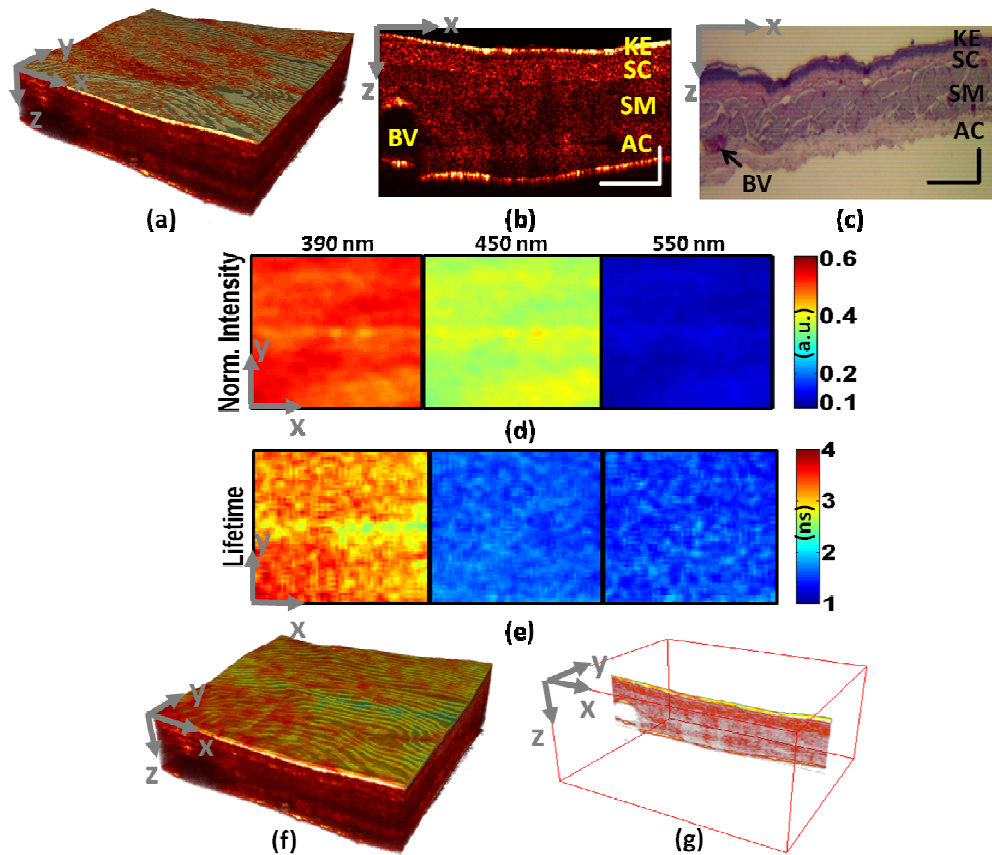

Fig. 5. Dual-modal OCT images and FLIM maps of *in vivo* normal hamster cheek pouch (2000 (x) x 2000 (y) x 450 (z) µm). (a) 3-D OCT volume, (b) 2-D OCT B-scan (KE: Keratinized stratified squamous epithelium, SC: subepithelial connective tissue (lamina propria), SM: skeletal muscle layer (tunica muscularis), AC: adventitial connective tissue, and BV: Blood vessel), (c) H&E histology corresponding to (b), (d) Normalized fluorescence intensity maps, (e) Fluorescence lifetime maps, (f) 3-D OCT/FLIM volume with a fluorescence lifetime map in 390 nm band, and (g) Ortho-sliced image from (f). Horizontal scale bar = 400 µm and vertical scale bar = 100 µm. Movies showing 3D nature of OCT/FLIM volume: Media 6 and Media 7.

The second example corresponds to a segment of oral mucosa presenting a squamous cell carcinoma (SCC) lesion, shown in Fig. 6. The OCT volume (2000 (x) x 2000 (y) x 650 (z) µm) in Fig. 6(a) showed a major lesion with a size of ~1500 (x) x 1000 (y) µm at the bottom and a small tumor-suspicious bump with a size of ~200 (x) x 200 (y) µm at the upper right corner. The thickness of the major lesion (~650 µm) and normal-like surrounding area (~250 µm) was visibly determined in a cross-sectional OCT B-scan along the main lesion (Fig. 6(b)), assuming the average tissue refractive index of 1.4. Degradation of the layered structures toward the major lesion and no layer at the lesion location was also observed

although OCT signal under the major lesion was weak due to low backscattering from the thick cancer lesion. Histopathology analysis of the imaged area confirmed that the major lesion corresponds to squamous cell carcinoma (SCC) (Fig. 6(c)).
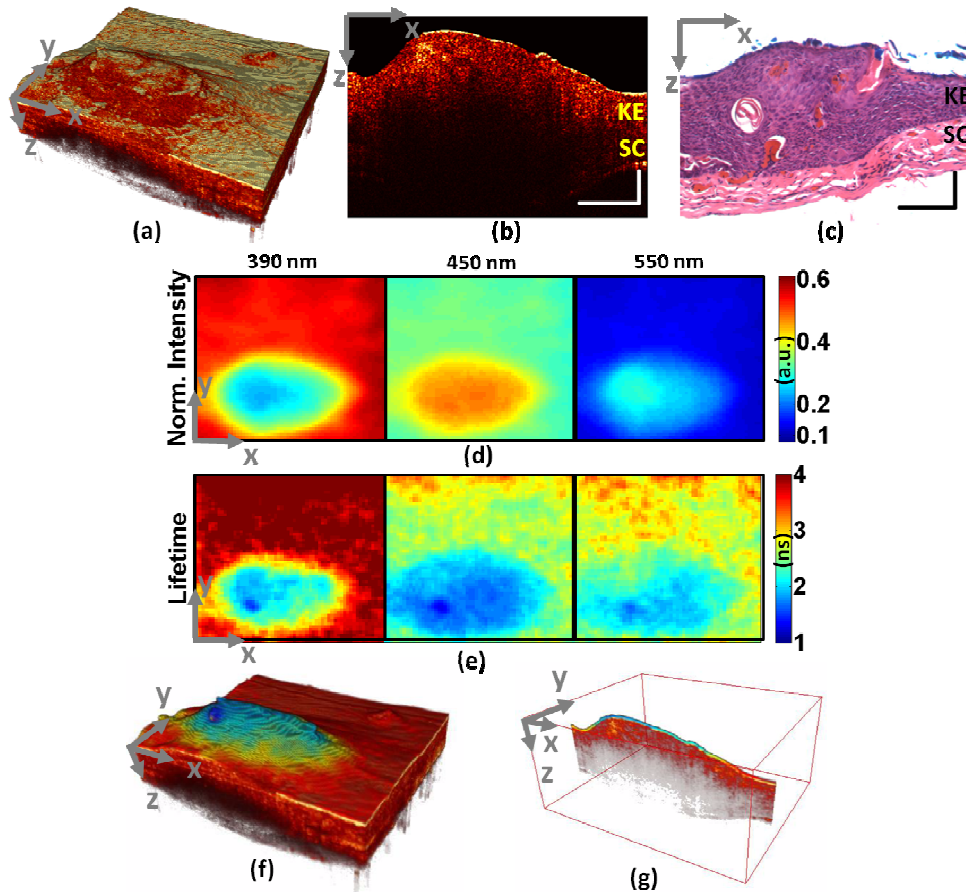

Fig. 6. Dual-modal OCT images and FLIM maps of *in vivo* cancerous hamster cheek pouch (2000 (x) x 2000 (y) x 650 (z) µm). (a) 3-D OCT volume, (b) 2-D OCT B-scan (KE: Keratinized stratified squamous epithelium, and SC: subepithelial connective tissue), (c) H&E histology corresponding to (b), (d) Normalized fluorescence intensity maps, (e) Fluorescence lifetime maps, (f) 3-D OCT/FLIM volume with fluorescence lifetime in 390 nm band, and (g) Ortho-sliced image from (f). Horizontal scale bar = 400 µm and vertical scale bar = 100 µm. Movies showing 3D nature of OCT/FLIM volume: Media 8 and Media 9.

The multispectral FLIM maps of the cancerous hamster cheek pouch are shown in Fig. 6 (d-e). The difference between the major lesion at the bottom and the surrounding area was detected in both the normalized fluorescence intensity and lifetime maps in all three bands. The normalized fluorescence intensity in the surrounding area was ~50% at the 390 nm band, ~40% at the 450 nm band and ~10% at the 550 nm band. Lifetimes in the surrounding area were ~3.9 ns at the 390 nm band, ~2.4 ns at the 450 nm band and ~2.7 ns at the 550 nm band. The normalized fluorescence intensity and the values of lifetimes resembled those of the normal oral mucosa containing collagen as the dominant fluorophore. In the major lesion, the normalized fluorescence intensity decreases to ~20% at the 390 nm band, and increases to ~55% at the 450nm band and to ~25% at the 550 nm band. The values of lifetimes were ~1.5 ns at 390 nm band, ~1.3 ns at 450 nm band, and ~2.1 ns at 550 nm band. The fluorescence characteristics of normalized fluorescence intensities and lifetimes resembled the emission of

NADH (at the 450 nm band) and FAD (at the 550 nm band), which are the dominant fluorophores of cancerous tissues [25].

In Fig. 6(f-g) we also show the normalized fluorescence lifetime map from the 390 nm band overlaid over the corresponding OCT volume of the imaged lesion and an ortho-sliced image. In these multimodal images we can clearly see two distinct regions showing very distinct morphology and biochemical composition, which are in agreement with the histopathological characteristics of a squamous cell carcinoma and benign tissue.

4. Discussion

The volumetric morphological OCT images and *en face* biochemical FLIM maps of biological tissues measured with the dual-modality instrumentation demonstrate the complementary nature of the two modalities. The morphological image of the atherosclerotic artery in Fig. 4(a-b) revealed the existence of a cap over a calcified necrotic core as well as the cap thickness. The biochemical maps Fig. 4(d-e) indicated a strong contribution from the structural protein collagen in the area surrounding the fibroatheroma and a strong lipid contribution directly above the necrotic core. Both morphological and biochemical observations are important criterion for classifying the plaque and clinical diagnosis. Similar results are available from the morphological and biochemical images of the squamous cell carcinoma. The size of the lesion and the breakdown of the tissue layer organization are evident in the morphological Fig. 6(a-b) image. The biochemical maps indicate an increased contribution from NADH and FAD (relative to the collagen contribution) in the area of the lesion compared to the surrounding area, likely indicating increased metabolism (Fig. 6(d-e)). Again both the morphological and biochemical observations are important for distinguishing a malignant carcinoma from a lesion due to benign causes such as trauma (scar tissue) and/or inflammation. While the dual-modality system clearly is able to deliver a more complete view of the optical response, the utility of the additional information for diagnosis will ultimately have to be proven by the more extensive studies underway.

The inherent multidimensional nature of the dual-modality data set posses a challenge for the effective visualization for diagnosis. Moreover, the visual interpretation of the biochemical maps could be enhanced by placing them in the context of the morphological image. As a first pass at visually integrating the morphological and biochemical images we have made projections of individual multispectral FLIM maps onto the OCT volume as shown in panels f and g of Figs. 3-6. In order to produce the integrated volumes the air tissue interface in the volumetric image had to be detected. Standard noise reduction (median, average and morphological filters) and edge detection algorithms (Sobel, Prewitt and Canny methods) were applied to the OCT data to detect the boundary. In most cases the boundary was successfully detected because of the strong reflection at the boundary, however the boundary in regions with low SNR or regionally saturated OCT data were not accurately detected. In these cases the border was determined by hand. The application of a more robust detection algorithm will be required in the future to suppress noise and circumvent the regionally saturated and low SNR data. We also explored color mapping for the two modalities since the morphological and biochemical information should be distinguishable in the image. Future iterations will try to combine the biochemical maps into some metric based upon the results of the two ongoing studies that will simultaneously reduce the data size and enhance the diagnostic value.

An important aspect of any imaging technology that is meant to ultimately find its way into the clinic is speed in data acquisition and processing. While the data acquisition speed of the prototype system was relatively fast, for clinical work it would be desirable to go even faster in order to avoid any issues with motion artifact. The OCT subsystem line rate could readily be increase to 70 KHz simply by replacing the current line-scan camera with more recent camera technology. We could go even faster if we adopted a swept laser source OCT approach and also improve the imaging depth by moving to longer wavelengths. The pixel rate of the FLIM acquisition could also be readily increased simply by the acquisition of a high pulse energy and high repetition rate excitation laser. Commercially available sources

with high repetition rates (>50 KHz) and high enough pulse energy (~4 μJ) to enable laser repetition rate limited FLIM imaging are readily available. As we have discussed previously [12], the resulting higher average power of the excitation laser will not push the laser fluence above the ANSI limit for skin exposure because of the much reduced dwell time. Based on these improvements, a 2x2 mm^2 area could be imaged in less than 600 ms.

The image processing for the prototype system was done in Matlab which is very versatile and easy to use, but not particularly efficient. OCT cross-sectional images are routinely processed in real time at over 30 frames per second using custom C code. Similarly, the inherent speed of the Laguerre deconvolution method [17] should enable FLIM map rendering in under 1 minute once the method is written into much more efficient C code. While the current image Matlab processing scripts are not fast enough to be used in the clinic, the path toward high speed image processing is straightforward and should enable image rendering in approximately 1 minute post acquisition.

6. Conclusion

We have developed a dual-modality OCT/FLIM imaging system to explore the hypothesis that a more complete survey of the optical response would significantly improve the diagnostic power for the early detection of pathological conditions. It is widely accepted that earlier diagnosis of most diseases will decrease the associated morbidity and mortality. OCT and FLIM were identified for combination because of the complementary nature of the OCT morphological images and the FLIM biochemical maps. Following validation experiments with known fluorophores and scattering media we have begun to test our hypothesis for the classification of atherosclerotic plaques and the diagnosis of oral cancer. Early results from ongoing studies involving the imaging of e*x vivo* human atherosclerotic coronary artery and an *in vivo* hamster cheek pouch model of oral cancer illustrated the complementary nature of the two modalities and how each contributes to the optical characterization of the sample.

Acknowledgements